Microgravity experiments and numerical studies on ethanol/air spray flames

Romain Thimothée, Christian Chauveau, Fabien Halter, Colette Nicoli, Pierre Haldenwang, Bruno Denet

C. R. Mecanique 345 (2017) 99–116

Contents lists available at ScienceDirect

Comptes Rendus Mecanique

www.sciencedirect.com

Basic and applied researches in microgravity/Recherches fondamentales et appliquées en microgravité

Microgravity experiments and numerical studies on ethanol/air spray flames

Romain Thimothée [a], Christian Chauveau [a], Fabien Halter [a], Colette Nicoli [b], Pierre Haldenwang [b], Bruno Denet [c]

[a] ICARE, CNRS, UPR3021, 1C, avenue de la Recherche-Scientifique, 45071, Orléans cedex 2, France
[b] Aix-Marseille Université, CNRS, Centrale Marseille M2P2, UMR7340, 13451 Marseille cedex 20, France
[c] Aix-Marseille Université, CNRS, Centrale Marseille IRPHE, UMR7342, B.P. 146, 13384 Marseille cedex 13, France

ARTICLE INFO

Article history:
Received 28 July 2016
Accepted 20 September 2016
Available online 16 November 2016

Keywords:
Spray flame
Two-phase combustion
Wilson cloud chamber principle
Droplet array combustion
Flame front instability

ABSTRACT

Spray flames are known to exhibit amazing features in comparison with single-phase flames. The weightless situation offers the conditions in which the spray characteristics can be well controlled before and during combustion. The article reports on a joint experimental/numerical work that concerns ethanol/air spray flames observed in a spherical chamber using the condensation technique of expansion cooling (based on the Wilson cloud chamber principle), under microgravity.

We describe the experimental set-up and give details on the creation of a homogeneous and nearly monosized aerosol. Different optical diagnostics are employed successfully to measure the relevant parameters of two-phase combustion. A classical shadowgraphy system is used to track the flame speed propagation and allow us to observe the flame front instability. The complete characterization of the aerosol is performed with a laser diffraction particle size analyser by measuring the droplet diameter and the droplet density number, just before ignition. A laser tomography device allows us to measure the temporal evolution of the droplet displacement during flame propagation, as well as to identify the presence of droplets in the burnt gases. The numerical modelling is briefly recalled. In particular, spray-flame propagation is schematized by the combustion spread in a 2-D lattice of fuel droplets surrounded by an initial gaseous mixture of fuel vapour and air.

In its spherical expansion, the spray flame presents a corrugated front pattern, while the equivalent single-phase flame does not. From a numerical point of view, the same phenomena of wrinkles are also observed in the simulations. The front pattern pointed out by the numerical approach is identified as of Darrieus–Landau (DL) type. The droplets are found to trigger the instability. Then, we quantitatively compare experimental data with numerical predictions on spray-flame speed. The experimental results show that the spray-flame speed is of the same order of magnitude as that of the single-phase premixed flame. On the other hand, the numerical results exhibit the role played by the droplet radius in spray-flame propagation, and retrieve the experiments only when the droplets are small enough and when the Darrieus–Landau instability is triggered. A final discussion is developed to interpret the various patterns experimentally observed for the spray-flame front.

E-mail address: romain.thimothee@cnrs-orleans.fr (R. Thimothée).

http://dx.doi.org/10.1016/j.crme.2016.10.013

1. Introduction

For the time being, the chemical storage of energy remains the only practical way to efficiently store energy. This concern stands well beyond the scope of on-boarding applications. Therefore, studying the combustion phenomena has to be considered as a major interest for numerous industrial processes, even though the combustion of fossil fuels is expected to disappear from the state-of-the-art techniques in the near future. Since chemical storage under liquid phase offers the best ratio in terms of energy to container weight, combustion of liquid fuels is expected to be involved in numerous applications of future industrial interest.

Two-phase combustion has already a long history, even when microgravity was involved. In the early 1980s, Ballal and Lefebvre [1] reported on two-phase flame experiments within the framework of a laboratory drop configuration. Nowadays, facilities for weightless experiments are multiple (drop tower, aircraft, rocket, space station) and offer a large microgravity time range from the second to the day. The microgravity results presented in the article have been obtained thanks to parabolic flights of the Airbus A310 ZERO-G of the CNES, which provide a weightless time of 22 s. On the other hand, most of the microgravity results on two-phase flames have been obtained in drop towers or mine wells. This is explained by the fact that the security requirements for non-flying apparatus are less demanding than for a flying set-up.

From the earliest experiments on two-phase flames, flame speed enhancement by the presence of droplets has often been observed. A summary of the first contributions has been carried out by Myers and Lefebvre (1986) [2]. For instance, the addition of kerosene droplets to a propane–air mixture increases the propagation speed of the flame, as observed by Cekalin (1961) [3] or by Mizutani and Nakajima (1973) [4] and [5]. It is moreover worth mentioning that the pioneering works of Hayashi and Kumagai (1975) [6] and Hayashi et al. (1976) [7] used a Wilson cloud chamber to produce a nearly monodisperse spray. These authors underlined the role of the droplet size on propagation. For polydisperse kerosene sprays, Polymeropoulos and Das (1975) [8] observed that burning velocity reaches a maximum for a certain domain of droplet size.

In a general manner, experiments of combustion in sprays at moderate or high pressures have revealed behaviours in large departure from the equivalent gaseous premixed flames. Two-phase flames have been found to propagate with a pulsating flame speed regime [9,10], which does not imply differential diffusive effects [11,12]. The recent experimental literature also reports on numerous situations where the spray flame is more corrugated, and propagates faster, than the equivalent single-phase flame. We have particularly in mind the recent experiments conducted in a Wilson chamber by [13] – these experiments being performed on the ground – and by [14] in micro-gravity. Consequent wrinklings have also been mentioned in earlier works about spray flames [7,15], or solid particle cloud combustion [10].

The full understanding of the velocity increase is, however, not achieved. For ethanol and iso-octane sprays, Hayashi and Kumagai (1975) [6] and Hayashi et al. (1976) [7] observed the promotion of speed for both rich sprays and lean sprays, when the droplet size is sufficient. But, Ballal and Lefebvre (1981) [1] for iso-octane, and Myers and Lefebvre (1986) [2] with six different fuels, did not observe the promotion of speed for lean sprays. More recently, results obtained in microgravity [16] have shown that spray flames in lean ethanol/air mixtures can propagate faster than the equivalent gaseous flames for a narrow range of droplet sizes, and slower in globally rich mixtures. Furthermore, classical ground experiments [7,13] have exhibited opposite observations to those made in [16]: spray flames in rich mixtures of ethanol (or iso-octane) and air are faster than the equivalent gaseous premixed flame. The recent numerical investigations on spray flames propagating through globally rich mixtures [17,18] have brought clarifications by describing the various effects played by the spray main parameters: φ_G, the equivalence ratio of the initial fuel-saturated premixture that surrounds the droplets before combustion starts, φ_L, the liquid loading or the equivalence ratio of the fuel under liquid phase to the overall quantity of air, and L_d, the typical interdistance between the droplets. We obviously have $\varphi_T = \varphi_G + \varphi_L$ (with φ_T the spray overall equivalence ratio).

On the other hand, in numerous experiments, the flame front was found corrugated, with a large number of cells. Therefore, spray-flame speed enhancement could possibly be explained by instabilities of the front. As a matter of fact, the interplay between instabilities and droplets seems to have a peculiar importance for the spherical flames, a case that has been focused on in the more recent years [19,20,13], either on the ground, or in microgravity. These experiments have clearly established that a flat spray flame is prone to be unstable.

Among the numerous issues addressed by the peculiar behaviour of the spray flames, the paper hence stresses on the experimental characterization, the analysis and the interpretation of the possible spray-flame speed enhancement, in comparison with the equivalent single-phase flame. Two possible mechanisms seemingly can cooperate for the flame velocity promotion: a) the folding of the flame front due to droplets is known to increase the flame speed, since flame front wrinkles increase the flame surface; b) even when the flame front remains planar, the spray flame can speed-up owing to an intrinsic property of the spray flames.

The interplay between the experiments and the numerical simulations permits the discrimination between both mechanisms. The paper is therefore organized as follows. The experimental set-up is described in Section 2, while the numerical modelling is presented in Section 3. The characterization of the spray flame wrinkles is addressed in Section 4. The quantitative comparison between experimental data and numerical simulations is conducted in Section 5.

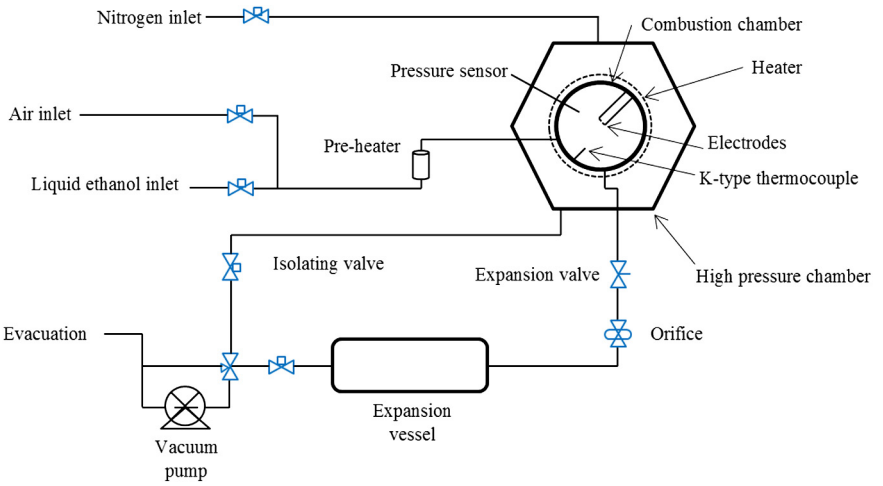

Fig. 1. Schematic representation of the experimental facility.

2. Experimental set-up

The present section is devoted to a brief presentation of the experimental set-up and our means of investigation. The basic configuration is a Wilson cloud chamber, which has been complemented by additional features essentially demanded by necessary security requirements for a flying apparatus.

2.1. Spherical aerosol flames of mono-sized droplets under microgravity condition

2.1.1. Dual chamber

A double confinement configuration was adopted in order to provide safe operating conditions, especially adequate for safety requirements on board the aircraft. It consists of a 1-litre spherical chamber, which is inserted in a high-pressure chamber of 11 litres. The inner chamber is filled with the flammable mixture, while the high-pressure chamber is simultaneously filled with nitrogen at the same pressure, thus ensuring proper sealing. The spherical combustion chamber is equipped with eight symmetrically distributed evacuation valves to release pressure during flame propagation. When the pressure inside the combustion chamber increases, the evacuation valves open and the remaining flammable gases are evacuated towards the high-pressure chamber to be mixed with nitrogen and ensure a totally inert mixture. Since the volume ratio of the outer to the inner chamber is about 10:1, the pressure increase is greatly alleviated, ensuring operational safety. A schematic of the experimental facility is given in Fig. 1.

Liquid fuel injection is performed using a multi-injection system with a switching valve that delivers an accurate volume of ethanol to obtain the targeted equivalence ratio. The fresh gases are heated by an electric heating cable that encircles the chamber. Additionally, a pre-heater is used to pre-vaporize the air–fuel mixture before its injection in the combustion chamber. The reader is invited to refer to a previous conference paper for more details about the design and the filling process of the present dual chamber apparatus [14].

2.1.2. Creation of the fuel aerosol

The fuel aerosol is generated from this gaseous air–fuel mixture using the condensation technique of expansion cooling (based on the Wilson cloud chamber principle [21]). This method is a well-established method to create monodisperse droplets with a narrow size distribution. For this, the inner chamber is connected to an expansion cylinder of 2.5 litres, initially vacuumed, via an expansion valve and an adjustable orifice (see Fig. 1). The opening of the expansion valve induces a fast pressure drop in the combustion chamber (pressure drop, denoted ΔP), also decreasing the temperature of the gaseous mixture. When the partial pressure of the fuel becomes greater than its saturation pressure, condensation occurs, causing the formation of fuel droplets. Once the target pressure has been achieved in the combustion chamber, the expansion valve closes. The heterogeneous mixture may then be centrally ignited using two tungsten electrodes.

A K-type thermocouple 13 µm in diameter and a pressure sensor monitor the temperature and the pressure during the filling process and during the expansion for aerosol formation. During expansion, only a part of ethanol is condensed to create droplets. In other words, at the moment of ignition, ethanol is present both in a gaseous phase and in a liquid state (droplets). Therefore, the overall equivalence ratio of the mixture φ_T is nothing but the sum of the liquid equivalence ratio φ_L and the gaseous equivalence ratio φ_G. The expansion process requires that a large amount of gases be evacuated in the expansion vessel. However, the overall equivalence ratio can be properly assumed to be constant. Both previous parameters are assessed from the temperature and pressure measurements using the ideal gas law and with thermodynamic considerations.

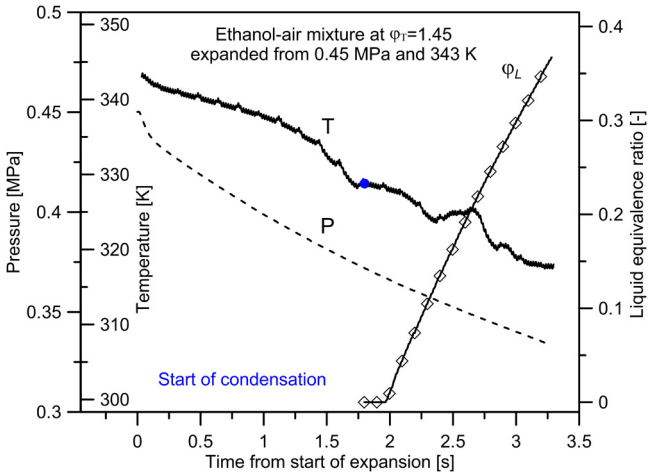

Fig. 2. Typical variation in pressure and temperature of the mixture inside the combustion chamber during expansion.

An example of typical pressure and temperature variations during expansion is shown in Fig. 2. The mixture at $\varphi_T = 1.45$ is expanded from $P_i = 0.45$ MPa and $T_i = 343$ K to the thermodynamic conditions of 0.33 MPa and 317 K. Condensation occurs at about 1.8 s after the beginning of the expansion and the liquid equivalence ratio sharply increases with time due to droplet formation, until it reaches a value near to $\varphi_L = 0.35$ at the end of expansion.

Two initial temperatures T_i of 334 K and 343 K were taken to allow reaching various couples of liquid and gaseous equivalence ratios. For combustion experiments, only the values of φ_L and φ_G prior to ignition (at the end of expansion) are considered as initial conditions for the aerosol.

2.2. Optical diagnostics

Two transparent windows on opposite sides of the high-pressure chamber (diameter 60 mm) aligned with two other windows on the combustion chamber (diameter 50 mm) allow optical access for diagnostics.

2.2.1. The shadowgraphy system

A classical shadowgraphy system is employed in order to track the flame front displacement and to visualize the flame surface. An Energetiq LDLS (Laser-Driven Light Source) is used as the light source, and a high-speed camera (Phantom v1210) continuously records the flame propagation at 15,000 fps (frames per second) with an image resolution of 768 × 768 pixels^2.

The temporal evolution of the flame radius $R_f(t)$ is obtained directly from the shadowgraph images where a post-processing program was used to fit the flame front, highlighted with a luminous zone, with a circle. The temporal derivation of the flame radius yields the propagation flame speed V_S such as: $dR_f(t)/dt = V_S(t)$. The unstretched propagation flame speed, noted V_S^0, is extracted by extrapolation to zero stretch of values of V_S versus the flame stretch rate $\kappa = 2 \cdot V_S/R_f$ using the non-linear model [22,23]. More details about this methodology can be found in [14].

The unstretched flame propagation speed is then used as flame speed parameter to compare the two-phase and gaseous flame speed. The shadowgraphy system also provides a qualitative information on the intensity and the development status of cellular instabilities on the flame surface, which is discussed in a later section.

2.2.2. Aerosol characterization prior to ignition

A relevant study of the aerosol impact on spherically propagating flames needs a complete characterization of the aerosol. The droplet diameter and the droplet number density, defined as the number of droplets per unit of volume, are characterized prior to ignition and during the aerosol formation using a laser diffraction particle size analyser (HELOS Sympatec). For each time step, a narrow size distribution of droplets is measured and the Sauter Mean Diameter D_{32} is selected as the mean diameter of the aerosol. The droplet number density is evaluated by measuring the laser attenuation signal and by using the Beer–Lambert law. More details about this method can be found in the previous contribution [24].

Fig. 3 shows typical temporal evolutions of the droplet number density (in log scale with blue solid line) and of the droplet diameter (black filled squares) during the expansion process for an initially gaseous ethanol–air mixture characterized by $T_i = 343$ K, $P_i = 0.4$ MPa, $\Delta P = 0.15$ MPa and $\varphi_T = 1.1$. Data acquisition is triggered by the opening of the expansion valve and only the time lapse from the beginning of the condensation is considered on the graph.

The droplet number density sharply increases and remains constant after a few seconds. The D_{32} increases due to droplet growing, to reach 15 µm at the end of the expansion process. Ignition is then triggered shortly after (with a time delay of 750 ms) to avoid vaporisation of the droplets due the warm wall of the chamber. For combustion experiments, the values of the diameter and of the number density prior to ignition are considered as initial conditions for the aerosol.

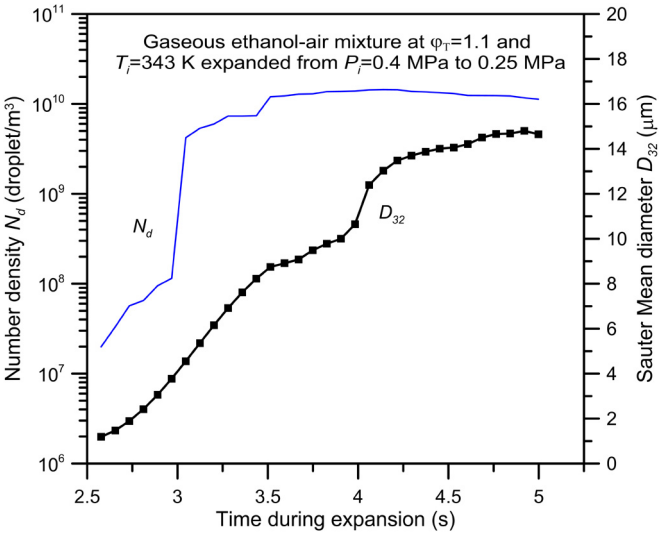

Fig. 3. Typical variations of the D_{32} and the droplet number density with time during expansion.

Droplet densities and mean diameters can be noticeably varied by changing the initial pressure P_i, the pressure drop ΔP and the initial fuel quantity φ_T. Basically, the D_{32} increases with the initial fuel quantity and is not significantly influenced by the initial pressure, although the number of droplets per unit volume increases with the initial pressure and remains roughly constant with the fuel quantity.

2.2.3. Laser tomography

A laser tomography device is employed for measuring the position of the droplets and for computing their radial displacement during combustion. A laser (Coherent Verdi) emitting a laser beam at 532 nm is used with an optical system consisting of adequate lenses to generate a thin laser sheet less than 250 μm in thickness at the centre of the combustion chamber. A light absorber disposed at the bottom of the combustion chamber limits the light reflections on the walls. A camera (Phantom v1611) focusing on the laser sheet and equipped with an interference filter at 532 nm receives the light scattered by the fuel droplets located in the laser sheet plane.

Examples of instantaneous laser tomography images during flame propagation are given in Fig. 4. Due to the spherical symmetry, only a quarter of each image is shown. Electrodes are located on the right and at the top of the frames, which are referred to by the times from the triggering of ignition. The experiment initial conditions are: $P_i = 0.40$ MPa, $T_i = 343$ K, $\Delta P = 0.15$ MPa, and $\varphi_T = 1.20$.

An acquisition rate of 19,000 fps and a spatial resolution of 768 $\times$ 768 pixels^2 corresponding to a 40.5-mm side enable a precise tracking of the temporal evolution of the position of fuel droplets during flame propagation. The evaluation of the radial displacement of each droplet, noted D_r, is performed using a PTV treatment [25] (Particle Tracking Velocimetry). The trajectory of an individual droplet is illustrated in the left-hand side of Fig. 5. Four positions of this droplet are shown on the graph and are also reported with a red cross on the laser tomography images presented in Fig. 4 in order to illustrate the tracking of the fuel droplet. When the flame propagates, fuel droplets initially motionless are set into motion by the expansion of the burnt gases. From the values of the radial displacement of each droplet, it is possible to evaluate a droplet velocity by applying the temporal derivative. The Stokes number has been calculated for several conditions of aerosol experiments and was found to be far lower than unity. Therefore, all droplets faithfully follow the gas flow and have low inertia.

Unlike the fresh gases that undergo the expansion of the flame, burnt gases are at rest if not affected by effects of radiation [26]. As a result, a particle crossing the reaction zone may be identified because of its change in velocity. An example of a such a measurement is shown in the right-hand side of Fig. 5 for the initial conditions $P_i = 0.60$ MPa, $T_i = 343$ K, $\Delta P = 0.25$ MPa, and $\varphi_T = 0.80$. For the sake of clarity, only the end of the droplet trajectory is reported on this figure. The droplet is moved over two millimetres by flame expansion. Then, its position remains unchanged during less than one millisecond. This droplet is located in the burnt gases, which is highlighted by the stagnation of the radial displacement ($\mathrm{d}D_r(t)/\mathrm{d}t = 0$).

It can be noted that measurements are performed until the luminous signal from the droplets disappeared, in other words, until droplets are fully evaporated. The droplet shown in the left-hand-side Fig. 5 is vaporized ahead the flame front during its displacement, while the droplet considered in the right-hand-side figure clearly crosses the reactive zone and is then vaporized in the hot burnt gases.

Using this criterion of droplet motion, two distinct behaviours of droplets ahead the flame can be identified. Firstly, droplets evaporate progressively ahead the flame front and do not cross the flame. Secondly, droplets cross the flame and

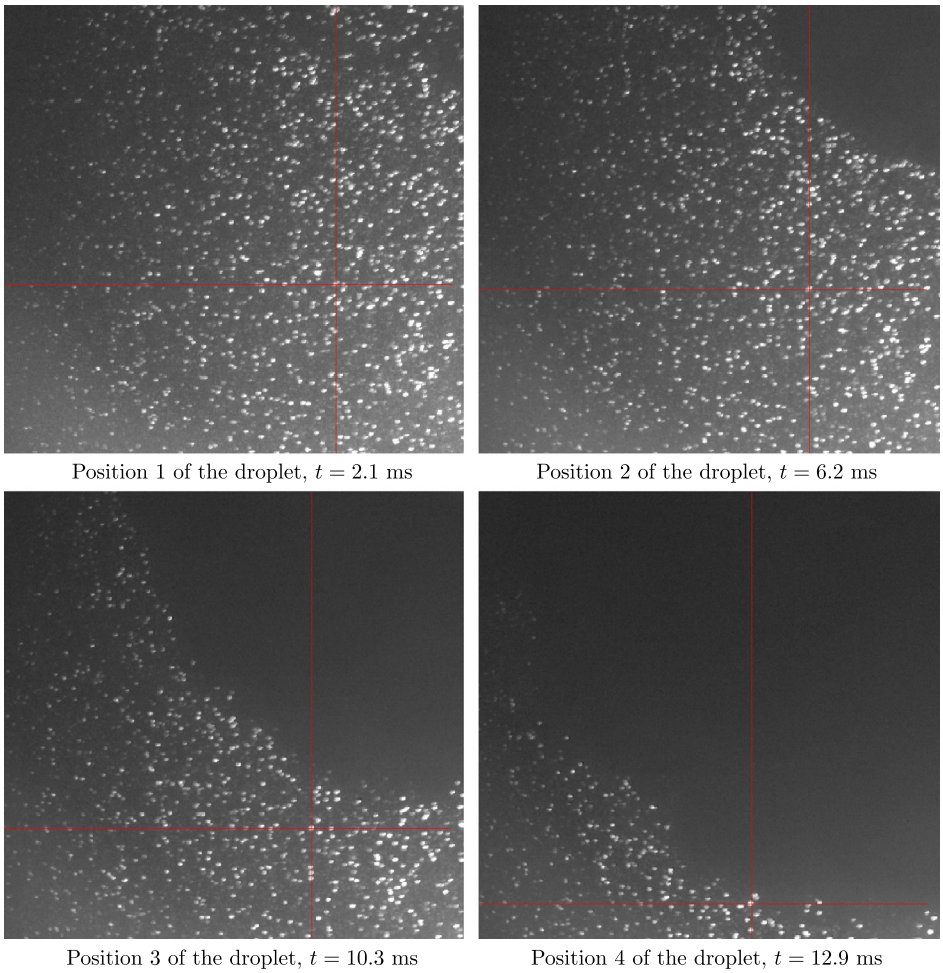

Fig. 4. Example of instantaneous laser tomography images at different instants (time is considered from the triggering of the ignition). The tracking of a given fuel droplet is also illustrated.

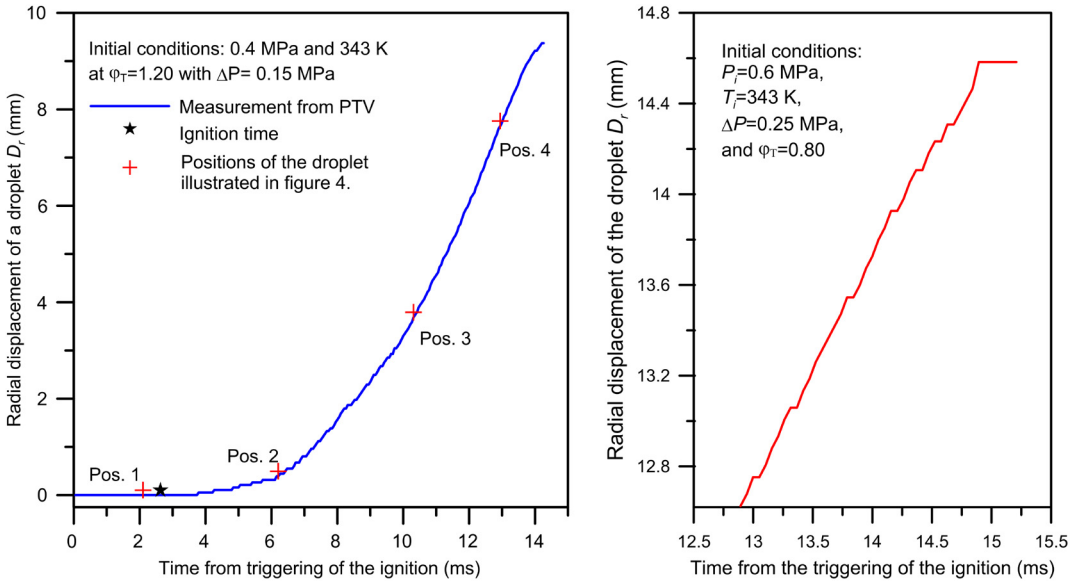

Fig. 5. Left: Measurement of the radial displacement of an individual droplet during flame propagation; Right: Example of a fuel droplet identified in the burnt gases with an immobility criterion.

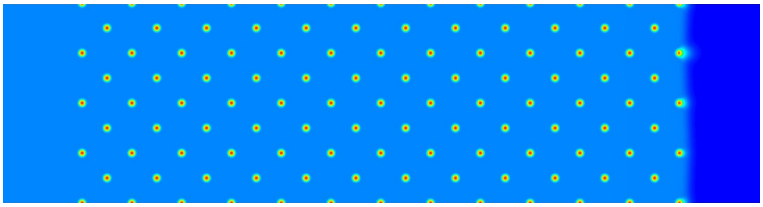

Fig. 6. 2-D lattice of ethanol droplets: fuel mass fraction resulting from the positioning of the droplets at the nodes of a 2D-lattice of spacing s. On the very right-hand side of the figure, a planar single-phase premixed flame propagates to the left (in the lattice: $\varphi_G = 0.66$, $\varphi_T = 1$, $s = 6$). The computational domain represented is $L_y = 4 \times s$ hight and $L_x = 14 \times s$ long.

are found in the burnt gases without any motion. The possible presence of droplets in the burnt gases will be discussed with two-phase flame instabilities in a forthcoming section.

3. Modelling spray combustion through a 2-D lattice of droplets

At moderate and high pressures, the spray-flame thickness is generally smaller than the average droplet interspacing. No process of homogenization is therefore permitted. In such a system where both phases are initially in equilibrium, the spray flame often tends to be controlled by vaporization, the chemical heat release allowing the vaporization of the droplets one after another. Therefore, the spray flame propagates within a heterogeneous (or stratified) mixture with vaporizing droplets. This is why an original chemical scheme dedicated to ethanol/air combustion has been developed for such non-homogeneous mixtures. The present ethanol/air system is directly inspired from what has previously been developed for decane [17].

3.1. Controlled initial state of the spray

The numerical approach starts from a spray system schematized as a set of individual ethanol droplets initially located at the nodes of a face-centred 2D-lattice, surrounded by a saturated mixture of ethanol and air. The lattice is conceived as a particular initial state of the fresh spray, since the droplets can move during the combustion process. Hence, the lattice of the droplets, as depicted by the field of fuel mass fraction drawn in Fig. 6, is a manner of controlling the spray's initial conditions. Other control attempts exist in the literature. For instance, Mikami et al. (2006) [27] measured the flame spread along an array of anchored n-decane droplets. In this microgravity experiment, the droplet size and the transverse interdroplet distance were fixed, only the interdroplet distance in the direction of spreading was changed. The purpose was to investigate different modes of droplet combustion, from individual to group combustion. The domain of overall equivalence ratio considered in [27] is much higher than the one studied here. Furthermore, the present numerical approach solves the vaporization and the combustion of "thick" individual droplets. This is in contrast to simulations that use point droplets, such as all 1D numerical studies on spray flame [28,29,11,30], or in the 2D analysis of [31]. The present approach fully resolves the droplets as in the numerical approach of [32]; here, we additionally allow the droplets to be carried by gas expansion.

3.2. Combustion for non-homogeneous mixture

The detailed chemical schemes for ethanol are too complex for efficient numerical simulations. This is why simplified chemical kinetics are generally recommended. It is long known that the classical one-step Arrhenius law (equipped with constant heat release) largely overestimates the adiabatic flame temperature on the rich side. To overcome the difficulty to assess the main rich flame characteristics (as speed and temperature), we have considered [33] a simple modification of the one-step chemical scheme: heat release becomes a function of the fresh mixture equivalence ratio, which is assessed with the use of two mixture fractions. In practice, this model is able to correctly mimic the premixed single-phase flame characteristics. The quantitative comparison with experimental data obtained with alkane (conducted in [34,17]) indicates that the model quite reasonably describes alkane spray combustion.

The contribution [17] (Appendix A) presents the whole system of the non-dimensional governing equations that are derived from the general laws of conservation. In the present article, the scales for non-dimensioning are now those of the stoichiometric flame of ethanol/air (flame thickness δ_f^*, transit time τ_f^*, adiabatic flame temperature T_b^*, and related density of the burnt gases ρ_b^*). The non-dimensional form of the heat equation deserves particular attention. It reads:

$$\frac{\partial \theta}{\partial t} + \mathbf{V}\cdot\nabla\theta = \frac{1}{\rho}\mathrm{div}(\rho\, D_{\mathrm{th}}\nabla\theta) + F(\varphi_u)\, W(\rho, \psi_i, \theta) \tag{1}$$

Devoted to energy conservation, equation (1) successively considers the budget of transport and diffusion and the production of thermal energy. The production of heat involves W, the rate of the chemical process, which is given by the standard

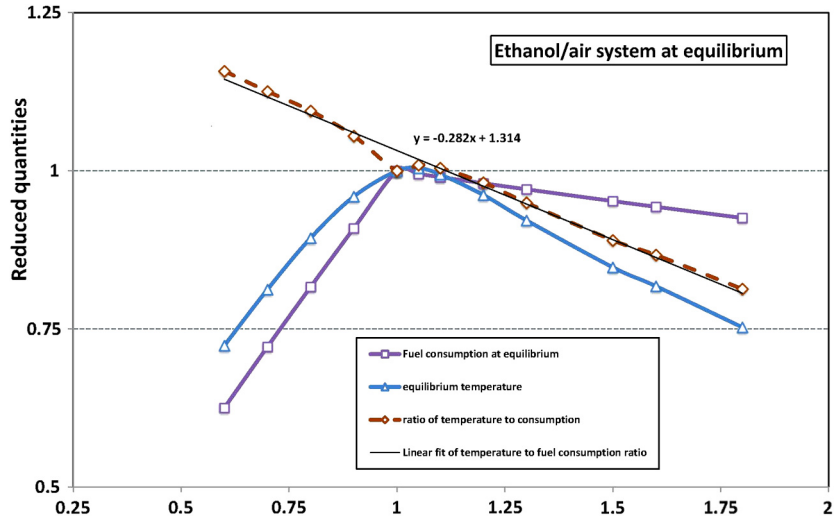

Fig. 7. Ethanol–air reactive system at equilibrium: the ratio of temperature to fuel consumption appears as a nearly-linear function of fresh air–fuel ratio.

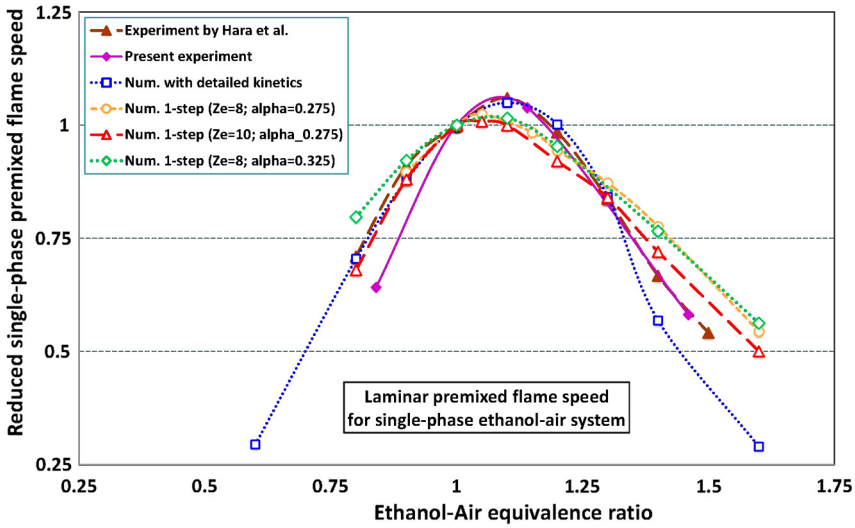

Fig. 8. Ethanol–air single-phase premixed flame speed as a function of premixture equivalence ratio, for various modelling parameters.

Arrhenius law, which depends on density, species mass fractions, and temperature. The latter dependence implies the choice of an activation temperature, which – when compared with the temperature of the stoichiometric premixed flame – leads to the selection of a Zeldovich number Ze. The additional factor $F(\varphi_u)$ allows the adaptation of the reaction heat to the actual chemistry. φ_u is the field of equivalence ratio upstream of the flame propagation. φ_u is derived from two combustion invariants [17]. F must be computed a priori for every chemical system as a function of the fresh mixture equivalence ratio φ_u; it accounts for the thermal energy produced by the fuel mass unit consumed at equilibrium. As indicated in Fig. 7, it turns out that the ratio of equilibrium temperature to fuel consumption is nearly linear, in such a way that we can write

$$F(\varphi_u) = 1 - \alpha(\varphi_u - 1) \quad \text{if} \quad \varphi_u \in]0.5, 2[\quad ; \quad F(\varphi_u) = 0, \quad \text{otherwise} \tag{2}$$

Accordingly with the slope of the linear fit in Fig. 7, a value of α around 0.28 will be retained. Furthermore, the model possesses the following additional ingredients. The fuel diffusivity is a strongly non-linear function of temperature, which prohibits the diffusion phenomena at low temperature and contains the liquid phase without the use of surface tension. In equation (1), **V** stands for the velocity field that is governed by the Navier–Stokes equations, solved under the approximation of low-Mach-number flow.

To end with the description of the model, and before coping with the simulation of spray flames, we need to validate the chemical approach with the single-phase classical premixed flame. The use of expression (2) in equation (1) allows us to provide an estimate of $U_L(\varphi_0)$, where φ_0 is the equivalence ratio of the fresh premixture. The comparison of the predicted flame speed with the experimental data, the present ones and those of the literature, is the purpose of Fig. 8. The sensitivity

with the parameters of heat release is additionally reported in the figure, where the effects of the variations in Ze and α are illustrated. We can notice the feeble effects on the single-phase flame speed induced by a 10% change in α, or by a 20% change in Ze.

3.3. Spray main parameters

The main parameters of the numerical schematization are s, the lattice spacing (in reactive–diffusive length units δ_f^*), L_y, the transverse size of the computational domain (in the same units), φ_{L}, the liquid loading (or equivalence ratio relative to the fuel under liquid phase), and φ_{G}, the gaseous equivalence ratio (i.e. that corresponding to the saturated vapour pressure in the fresh spray). From these parameters, we can easily determine the droplet radius R_{d} and the typical droplet interdistance L_{d}. Note that the lattice is at least L_y-periodic in the y-direction.

The numerical experiments are conducted as follows. The droplets are initially positioned at the nodes of a face-centred lattice of spacing s, as illustrated in Fig. 6. The lattice is embedded within a computational box of length L_x and height L_y. For periodicity reasons, we have chosen either $L_y = s$, $L_y = 2s$, or $L_y = 4s$. The surface tension of the droplets being neglected, the droplets appear as a dense fuel puff belonging to the same continuum as their surrounding premixture. Vaporization, and the Stefan flow in particular, are treated at the level of the conservation laws, and resolved numerically. Vaporization and the related gas expansion start when the medium is heated by the proximity of the flame.

3.4. Burning droplets of moderate size

First of all, let us define what is a droplet of large size. In both contributions [17,18], we have established that, when the "spray Péclet number" Pe_s is large, the fuel in a liquid phase does not participate in spray flame propagation. We recall that the "spray Péclet number" is defined as follows:

$$Pe_{\mathrm{s}} \propto \frac{\rho_L}{\rho_G} \frac{2R_{\mathrm{d}} \times U_L(\varphi_G)}{D^*_{\mathrm{th,b}}} \frac{2R_{\mathrm{d}}}{L_{\mathrm{d}}} \tag{3}$$

The "spray Péclet number" corresponds to the ratio of the droplet vaporization time $\tau_{\mathrm{vap}} \propto (\rho_L/\rho_G)(2R_{\mathrm{d}})^2/D^*_{\mathrm{th,b}}$ to the propagation time $\tau_{\mathrm{prop}} \propto L_{\mathrm{d}}/U_L(\varphi_{\mathrm{G}})$, where $U_L(\varphi_{\mathrm{G}})$ and $D^*_{\mathrm{th,b}}$ are the laminar single-phase flame speed related to the initial fuel-saturated mixture and the thermal diffusivity in the burnt gases of the stoichiometric single-phase laminar flame, respectively. When the "spray Péclet number" is large, flame propagation between two droplets is so fast that droplet vaporization does not modify the initial premixture that surrounds the droplets. In other words, the spray-flame speed is simply the one of the single-phase flame propagating in the initial premixture (i.e. $U_{\mathrm{S}} = U_{\mathrm{L}}(\varphi_{\mathrm{G}})$). This result has numerically been established clearly, as long as the spray flame remained planar [35]. This result allows us to predict that a spray with large droplets can remain flammable even with a large φ_{T}, provided that the premixture with φ_{G} can burn.

On the other hand, a spray with small droplets corresponds to situations where the vaporisation time is much smaller than the chemical time. In that case, Da, the Damköhler number, is supposed to be small; this implies that $\tau_{\mathrm{vap}} \ll \tau_{\mathrm{react}}$, and the spray-flame speed is found to be the same as the single-phase premixed flame (i.e. $U_{\mathrm{S}} = U_{\mathrm{L}}(\varphi_{\mathrm{T}})$) [11].

Beyond both limit cases, a spray with $Pe_{\mathrm{s}} \leq \mathcal{O}(1)$ and with $Da \geq \mathcal{O}(1)$ is said to be comprised of moderately sized droplets. In other words, vaporization always participates in propagation. Therefore, the droplet vaporization time (and hence the droplet mean radius) plays a role in the spray-flame speed. In the case where the vaporization fully controls the spray flame, the spray-flame speed decreases in inverse ratio to R_{d} [11,17]. The situation studied in the present paper remains quite far from this limit, since it will be measured that the spray-flame speed remains of the same order as the single-phase premixed flame, although it will be observed that the droplets can fully vaporize when crossing the spray flame.

4. Droplets increase the existence domain of front instabilities

The present section points out that spray flames are more prone to fold than the single-phase flame of the same overall equivalence ratio. Experimental analysis and numerical predictions strive towards the identification of the mechanism responsible for instability.

4.1. Domain of corrugated flames in the spherical bomb

This section presents experimental results and conducts a qualitative comparison between two-phase and homogeneous phase flames. The domain of stability/instability of the gaseous air–ethanol mixture is first investigated with a pressure–equivalence ratio diagram. Various initial pressures and equivalence ratios were explored with φ varying from 0.6 to 1.6 and P_i varying from 0.1 to 0.7 MPa. The gaseous combustion experiments were performed in the dual chamber by following the same procedure as described above, but without the prior expansion process. For the single-phase flame, the identification of the status with respect to stability is performed with the shadowgraphy system by comparing the flame surface at the same flame radius (taken near to the maximum radius permissible by the optical device). Fig. 9 shows the results

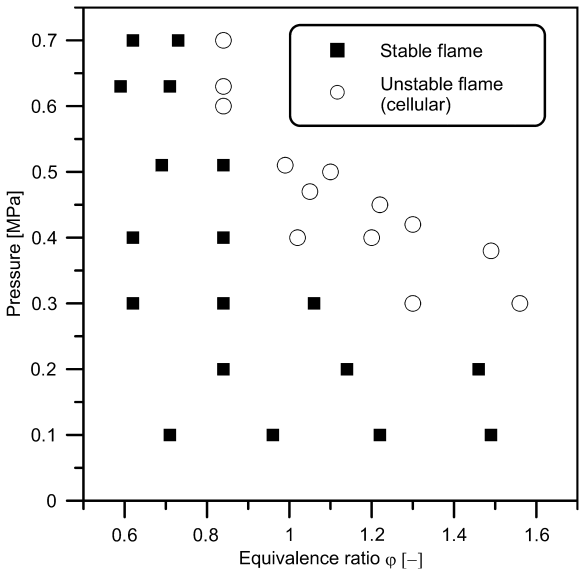

Fig. 9. Stability diagram of single-phase ethanol–air flames carried out at 334 K.

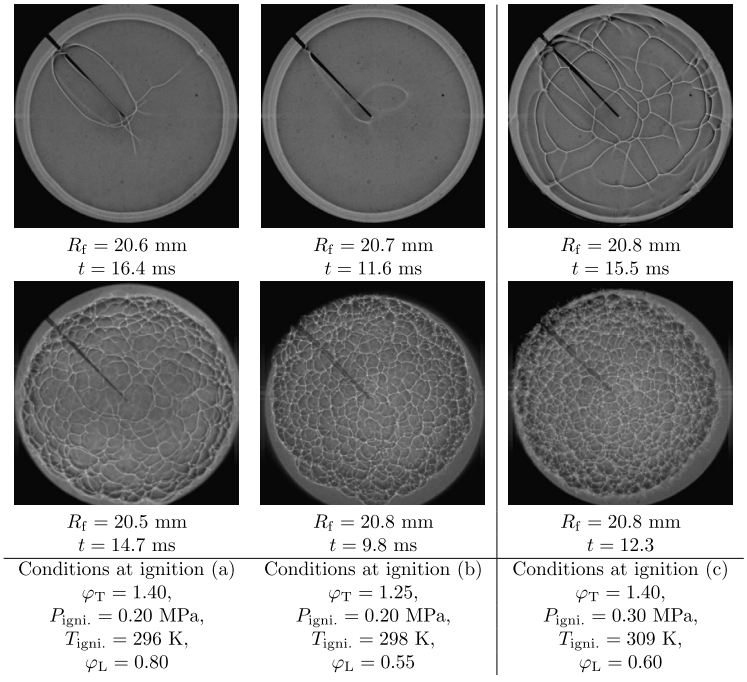

Fig. 10. Sequences of shadowgraphy images of aerosol flames compared with gaseous flames.

of observations obtained for an initial temperature of 334 K. This diagram is then used to select the conditions of pressure at ignition and overall equivalence ratio for the two-phase experiments. The impact of the presence of fuel droplets on an initially stable gaseous mixture and on a potentially unstable gaseous mixture is thus investigated.

Due to expansion, the temperature at ignition is always lower than the initial one. However, for the qualitative comparison of flame morphologies, the temperature effect on the onset of instabilities is assumed to be negligible. Fig. 10 shows results of morphology comparison between two-phase flames (second row) and gaseous flames (first row) reproduced at 334 K and at the same overall equivalence ratio and same ignition pressure. The frames presented are the results of three repetitive experiments, which are found similar. Flame radii and times of the flame observation are also indicated.

The two-phase flame shown in conditions (a) is obtained by expanding a gaseous mixture from $T_i = 343$ K and $P_i = 0.40$ MPa with $\Delta P = 0.20$ MPa. Flames shown in conditions (b) [respectively (c)] come from gaseous mixtures at $T_i = 334$ K, with $P_i = 0.35$ MPa [resp. $P_i = 0.40$ MPa] and with $\Delta P = 0.15$ MPa [resp. $\Delta P = 0.10$ MPa]. The resulting pressure with the

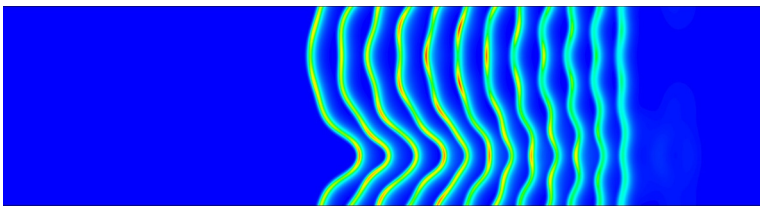

Fig. 11. Superimposed successive snapshots of the reaction rate for the spray flame subjected to DL-instability that has been triggered by ethanol droplets ($\varphi_G = 0.66$, $\varphi_T = 1$, $s = 6$ and $L_y = 24$, flame propagates from right to left).

corresponding temperature at ignition is reported in Fig. 10 with the overall and the liquid equivalence ratio. The latter quantifies the liquid quantity condensed into droplets just before ignition.

The results of Fig. 10 show that when the gaseous environment is totally stable, characterized by a smooth flame surface, the presence of fuel droplets conducts the flame to develop cellular instabilities on its flame. It is worth to be noted that the small cracks visible on the surface of the gaseous flame in the first column are due to the presence of the electrodes. Moreover, when the gaseous mixture can be unstable, as can be seen in the last column, the equivalent two-phase flame is also unstable, but with a more pronounced cellular intensity. Thin structures appear on the two-phase flame surface, giving a corrugated aspect to the spray flame. Basically, the presence of fuel droplets in a gaseous environment increases the onset domain of cellular instabilities.

4.2. Numerical simulation of droplet-triggered Darrieus–Landau instability

The numerical experiment consists in igniting the ethanol–air system described by Fig. 6 with the use of a thermal profile, hot only on the very right-hand side of the figure, as close as possible to the first row of droplets. The heat release appears as a slightly corrugated line, as shown by the first nearly vertical line of Fig. 11, starting from the right. The corrugations express the role of the droplets on the initially planar flame front. As a matter of fact, Fig. 11 superimposes twelve successive images of heat release, the spray flame propagating from right to left. We can notice that after spreading of a few tens of flame thickness, the spray flame adopts the classical cusped form of a front affected by the Darrieus–Landau (DL) instability, plus the prior corrugations due to the droplet impact. This numerical experiment calls for the following comments.

Remark 1. In the present numerical experiment, the vertical size of the computational box is $L_y = 24$. If the same experiment were performed with $L_y = 12$, only the light corrugations due to the droplet impact would appear. This is a characteristic of the Darrieus–Landau (DL) instability, which demands a computational box, transversally large enough to develop the instability [36], which then gives birth to the cusped form in the non-linear regime. For the present system, the cut-off length has been estimated at about $L_y = 15$.

Remark 2. It is long known that the DL-instability acts as a noise amplifier. In other words, to trigger DL-instability in single-phase premixture, the presence of initial perturbations is required. If the same experiment were performed without droplets, the DL-instability would develop only if the initial data were containing perturbation of sufficient level. This is again a characteristics of the Darrieus–Landau instability [36].

Remark 3. For a given box size, the larger the droplets are, the more sensitive the front is to DL instability.

Following the above analyses on the numerical results, we can conclude that the droplets act as initial disturbances, that trigger the Darrieus–Landau instability, which is here clearly identified.

4.3. Identifying the spray flame instability

We think that the above numerical results now help us to identify the nature of the instability that affects the spherical flame observed in the bomb. Two classical types of instabilities can affect the flat flames: the Darrieus–Landau (or hydrodynamic) instability and the diffusive-thermal instability. In the present numerical simulation, as we have no light species (with a small Lewis number) in our chemical scheme, the only instability of diffusive-thermal type that might be simulated is the oscillatory one for large Lewis number. This instability was not observed in our results. Therefore, we must turn towards the DL-instability.

In the pictures of Fig. 10 that concern spray flames, the typical size of the cells is about two millimetres. The Darrieus–Landau instability is known to fold the flame front with cells, the size of which is several tens of times the flame thickness. On the other hand, the flame thickness at pressures between 2 and 3 bar corresponds to a range lesser than 100 µm. Therefore, the typical size of the cells in Fig. 10 argues for the DL-instability. Moreover, if we look at the variation of the typical cell size with pressure or spray-flame speed, we observe that the cell size clearly diminishes as pressure increases

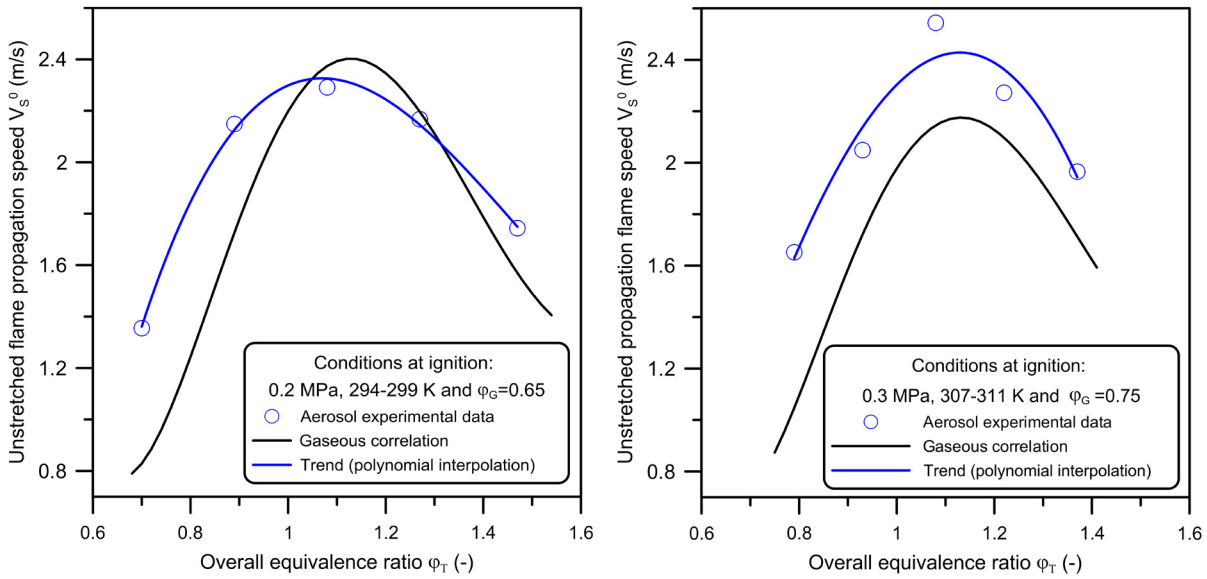

Fig. 12. Comparison between the two-phase and single-phase flame-speed parameters against the overall equivalence ratio.

(right snapshot), or as velocity is promoted (middle snapshot). In other words, the cell size strictly follows the variation of the flame thickness.

The Darrieus–Landau instability is known to be initially fed by noise. This point has been confirmed by the present numerical simulations, since the droplets brought perturbations to the flat flame, which were strong enough to trigger the DL-instability. Moreover, in the experiments, there are residual perturbations that can become sufficient – in strength and length scale – to trigger the DL-instability. This is what could happen in Fig. 9 for the lean single-phase mixtures, where pressure must increase to compensate the flame thickness increase due to the reduction in flame speed. Lastly, as the DL-instability increases the effective flame surface, a DL-affected flame should be faster than the same flat flame. This last point will intervene in the following section.

5. Assessment and comparison of the two-phase flame speed with the single phase flame speed

The purpose of the present section first concerns the experimental measurement of the velocity of the spray flame. The comparison between the data from the experiment and the numerical prediction is then conducted.

5.1. Experimental observation and flame-speed measurement of a two-phase flame

An important focus of this study is to compare both two-phase and gaseous flame speeds. The flame speed is one of the primary characteristics that describe a flammable mixture of a certain fuel in given conditions of temperature, pressure and equivalence ratio. The unstretched flame propagation speed V_S^0, introduced in section 2.2.1, is thus employed to investigate the impact of the aerosol on the laminar flame propagation. Values of unstretched flame propagation speed for the heterogeneous mixture are obtained by using the shadowgraphy system. For the gaseous cases, the flame speed parameter has to be determined under the same conditions than the ignition conditions of the two-phase mixture: overall equivalence ratio φ_T, temperature and pressure at ignition, $P_{igni.}$ and $T_{igni.}$. Due to the expansion process, the temperatures at ignition $T_{igni.}$ are low and strongly dependent on the initial temperature and the initial pressure, and the pressure drop. It, however, slightly depends on the equivalence ratio. For this reason, the unstretched flame propagation speeds of the gaseous cases are evaluated according to a flame-speed correlation established in a previous work [14].

The Fig. 12 compares both single-phase and two-phase flame speeds (a similar comparison has already been presented in a previous contribution [14]). Two pressure conditions at ignition of 0.20 and 0.30 MPa are carried out with a pressure drop (ΔP) of 0.15 and 0.10 MPa, respectively. Both pressures are maintained constant for all overall equivalence ratios. This leads to a roughly constant temperature at ignition and to a near-constant gaseous equivalence ratio of 0.65 and 0.75. The slight variation of the final temperature after expansion is due to the change in the overall equivalence ratio. The droplet density number is constant at $N_d = 6 \cdot 10^{10}$ m^{-3} [resp. $N_d = 7 \cdot 10^{10}$ m^{-3}] for the first [resp. second] aerosol conditions. An increase in droplet diameter from 10 to 16 µm and from 12 to 18 µm was measured for the ranges $\varphi_T = 0.7 - 1.5$ and $\varphi_T = 0.8 - 1.4$, respectively, and for the left-hand-side and right-hand-side graphs.

The flame speed values for the two-phase cases are average values of three experiments performed consecutively under reduced gravity conditions. The results displayed in the figure clearly demonstrate that, in most cases, a flame propagating

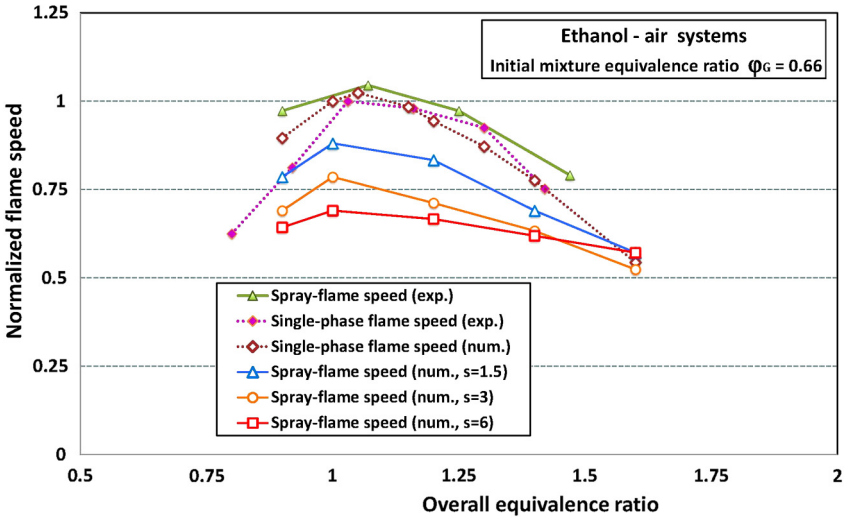

Fig. 13. Single-phase flame and spray flame normalized speeds as a function of the overall equivalence ratio: comparison between the experimental data and the numerical results for various lattice spacings s ($\varphi_G = 0.66$).

through a two-phase mixture propagates faster than in the equivalent single-phase mixture. The maximum difference between the two-phase and the single-phase flame speeds is observed for the leaner cases, with respectively about 0.4 m/s and 0.8 m/s for the first and the second graphs.

Two major phenomena could explain this flame speed promotion. First, a local enrichment created around each droplet during evaporation, which can conduct the flame to propagate in zones where the local equivalence ratio is nearer to the stoichiometry. Secondly, the pebbled aspect of the two-phase flame, which greatly increases the flame surface and thus increases the exchange surface between the fresh mixture and the reactive zone. The burning rate would consequently be greatly enhanced.

5.2. Comparison with the numerical predictions

When a flame front is strongly curved or corrugated, the determination of the instantaneous flame speed becomes not easy. We define the flame location as follows. We first choose an averaged definition of the front position by performing the partial integration of the temperature field in the transverse (periodic) y-direction. We hence obtain the one-dimensional quantity $< T >_y (x)$. We then define x_F, the front position, as the locus where $< T >_y (x_F) = 0.5$. Then, the slope of x_F, the front mean x-positioning, vs. time within the lattice is hereinafter called spray-flame speed. During the front travelling within the lattice, dx_F/dt admits a clear mean value, only slightly affected by the meeting of new droplets. This is the latter mean value, which is now compared with the experimental data.

In the experiments, the droplet size varies in the range [10 µm, 20 µm], giving a droplet interdistance approximately in the range [100 µm, 200 µm]. In our schematization with a lattice, this corresponds for s, the lattice spacing, to the range $\{3 \leq s \leq 6\}$. The first numerical results concern the velocity of a spray flame that remains flat, i.e. a simulation within a computational box with $L_y = 12$. The Fig. 13 gathers both experimental and numerical data of front speed against the equivalence ratio, for various values of s. The excellent agreement between the single-phase flame speed actually results from the construction of the numerical model. As for the spray flames, we notice that the numerical predictions get closer and closer to experimental measures, as s decreases. In other words, since the droplet vaporization intervene in the composition of the burning mixture, s (or the droplet radius) controls the vaporization time, and hence plays a role on the spreading rate. Unfortunately, even when s becomes much smaller that the actual values, the flat spray-flame speed is lesser than the experimental measure. In this way, accordingly with the numerical simulations, it lacks a decisive argument that would explain why the spray-flame speed is so close to the single-phase flame speed in Fig. 13.

As mentioned before, the spray flames are rarely flat. Droplet induced DL-instability increases the flame surface. The typical increase in surface can be of the order of 30%, so that the speed-up of the actual spray flame can be of 30% with respect to the flat spray flame. To sustain and illustrate the point, we have simultaneously drawn in Fig. 14 two pictures, namely, a picture that shows the various successive front patterns, using numerous snapshots of the reaction rate field, and a graph that depicts the mean front position, the slope of the latter curve giving the front velocity. Hence, the mean velocity that corresponds to a particular flame pattern can be read on the position curve, as the slope of the curve vertically below the considered pattern. Fig. 14 invites us to identify three different periods when the front propagates: from the right to the left of the figure, we notice:

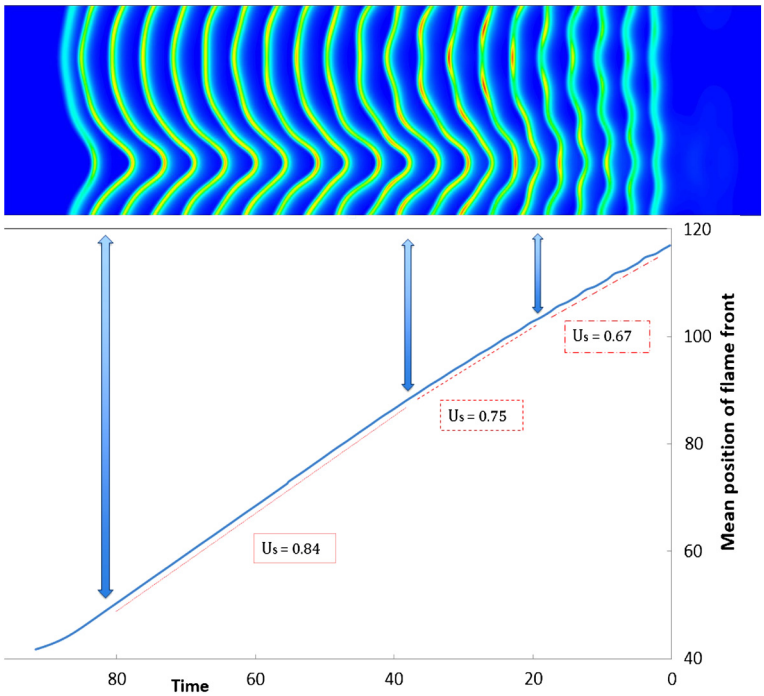

Fig. 14. Superimposition of twenty-one snapshots of the reaction rate field, positioned above the plot of the mean flame location, in such a way that the instant of each snapshot can be read on the time abscissa of the mean front location curve; three zones of particular flame speed are pointed out; parameters are $L_y = 4s = 24$, $\varphi_G = 0.66$ and $\varphi_T = 1$.

– a first time during which the spray-flame speed remains constant at about the speed of the planar spray flame $U_s = 0.67$ as given in Fig. 13 for $s = 6$ and $\varphi_T = 1$. During this short time lapse, the spray flame is perturbed by the droplet, and DL-instability starts to grow;
– a second period where the previous perturbations trigger an instability of much larger amplitude and length scale, namely the Darrieus–Landau instability, which superimposes on the droplet-induced pattern. It corresponds to a period of flame speed increase;
– a third time during which flame propagation attains a quasi-steady state of high velocity, i.e. $U_s = 0.84$. The front pattern corresponds to the classical DL corrugations which are now of maximum amplitude.

At the end of the above sequence, the flame leaves the region occupied by the droplet lattice, and becomes a slow single-phase flame, which appears as stable against the DL-instability. The analysis shows that the DL-instability can increase the spray-flame speed by 25%. This increase in spray-flame speed is enough to make numerical results and experimental data much closer in Fig. 13.

Furthermore, a recent contribution [35] has shown that large enough droplets, not only trigger the DL-instability, but also induce additional wrinkles on the DL-folded spray-flame pattern. These secondary corrugations are of shorter length scales. It ends up with an additional increase in the spray-flame surface, hence in spray-flame speed. This non-linear interplay between droplets and DL-pattern can lead to an overall increase of 50% with respect to the flat spray flame. The latter additional increase is not present here because the droplets are not sufficiently large.

6. Further discussion on cellular spray flames

The reality of a spray can be far from the present schematization with a lattice. Even though the average values can be identified, the lattice cannot contain any statistical disorder. It is however expected that any disorder can modify the properties of the percolation front: the droplets can be locally gathered in such a way that the local composition after vaporization can randomly be more – or less – favourable to propagation, and produces a net macroscopic propagation speed-up. This issue indeed stands well beyond the scope of our numerical simulations.

In terms of DL-pattern, it seems that such a disorder also plays a role in the design of the wrinkles. In what follows, we describe the relation experimentally observed between the spray-flame morphology and the fuel droplets crossing the flame front. Various scales of DL-instability in terms of cell size can seemingly be triggered according to the nature of the perturbations initiated by the droplets and is strongly dependent on the droplet interdistance.

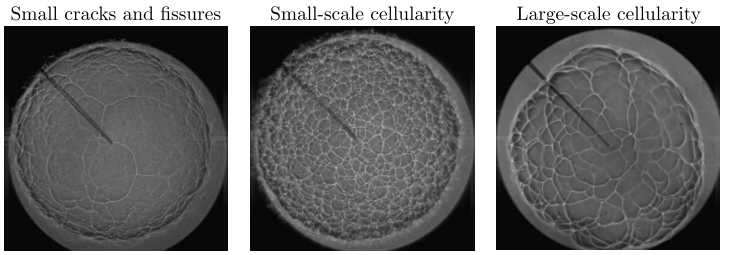

$R_f = 20.4$ mm $t = 8.6$ ms	$R_f = 21.0$ mm $t = 9.2$ ms	$R_f = 19.8$ mm $t = 18$ ms
Conditions at ignition (d) $\varphi_T = 0.90$, $P_{igni.} = 0.20$ MPa, $T_{igni.} = 295$ K, $\varphi_L = 0.30$	Conditions at ignition (e) $\varphi_T = 1.10$, $P_{igni.} = 0.30$ MPa, $T_{igni.} = 309$ K, $\varphi_L = 0.30$	Conditions at ignition (f) $\varphi_T = 1.60$, $P_{igni.} = 0.20$ MPa, $T_{igni.} = 307$ K, $\varphi_L = 0.50$

Fig. 15. Classification of the main types of two-phase morphologies characterized in terms of number and size and cells observed on the surface of the flame.

6.1. Cellular pattern with respect to droplet size

We propose to examine the possible relation between the crossing – or not – of the fuel droplets through the flame front and the morphology of the two-phase flames. Several experiments with aerosol flames have been explored at an initial temperature of 343 K, various conditions of initial pressures (P_i between 0.35 MPa and 0.60 MPa), of pressure drops (ΔP between 0.15 MPa and 0.3 MPa), and overall equivalence ratios (φ_T from 0.70 to 1.45). So a large range of mean diameters (D_{32}) between 5 and 23 µm and of droplet number densities from $1.5 \cdot 10^{10}$ m^{-3} to $2.0 \cdot 10^{11}$ m^{-3} was investigated.

Three main types of morphologies of two-phase flames have been identified experimentally using the shadowgraphy system. Illustrations given with images of shadowgraphy observation are presented in Fig. 15. The spray flames are documented with the flame radius and the corresponding time, with overall equivalence ratio, pressure and temperature just before ignition and liquid equivalence ratio. Three distinct morphologies are identified from the left to the right as: small cracks and fissures; small scale cells and large scale cells. This classification was performed qualitatively according to the intensity of instability expressed in terms of number and size of cells.

The PTV treatment applied to the images of laser tomography, as described in the section 2.2.3, allows us to classify all aerosol flames in terms of droplet front crossing, by using the criterion of particle motion. All two-phase conditions explored were thus clearly associated with the states 0 (no droplet crossing the flame front) and 1 (droplets crossing the flame front). The microgravity experiments of aerosol flames with laser tomography were performed separately from shadowgraphy. Nevertheless, the cycle-to-cycle repetition of aerosol formation is nicely repeatable.

The three morphologies of two-phase flames are mapped in a diagram together with the boundary of the two states in crossing for droplets. State 0 and state 1 can also be associated respectively with a complete evaporation and an incomplete evaporation of the droplets ahead the flame front. The results are shown in Fig. 16, where two different normalizations of the droplet radius are used. The vertical axis corresponds to the ratio of the Sauter Mean Diameter of the aerosol D_{32} to the average droplet interdistance, denoted a. In case of a highly diluted aerosol (the volume of the liquid phase being much smaller than that of the gaseous phase), the droplet mean interdistance can be estimated using the droplet number density, as $a \sim N_d^{-1/3}$ [37]. The D_{32} values are obtained from the measurements performed with the laser diffraction technique. On the other hand, the horizontal axis corresponds to the ratio of D_{32} to the laminar flame thickness δ_L^0, based on the maximal temperature gradient, the latter being assessed using the PREMIX code of CHEMKIN and with the kinetic scheme of ethanol oxidation of Leplat et al. [38] in aerosol thermodynamic conditions (pressure and temperature prior ignition) and for the overall equivalence ratio of the mixture, φ_T.

The repeatability of the results was ensured by conducting 3 successive experiments for each condition. The boundary between state 0 and state 1 of the droplets crossing is shown with a black line. The stable two-phase flames are represented with black points, and the stars illustrate the two-phase flames, which are unstable with: the red ones for small cracks and fissures; the blue ones for small-scale cellularity and the green ones for large-scale cellularity (which can be found in Fig. 15 from left to right).

The diagram of Fig. 16 shows that most of the flame morphologies observed are of small-scale cellularity type (blue stars), like the flames presented in Fig. 10. This type of instability has been associated with the D–L mode in the previous section 4.3. This diagram also indicates that flames with this small scale cellularity are located in the zone of crossing droplet and for aerosols with the largest droplet sizes (highest values of D_{32}/a) and flames with the lowest flame thicknesses (highest values of D_{32}/δ_L^0). This experimental result agrees well with the numerical analysis deduced in the sections 4.2 and 4.3. Fuel droplets that cross the flame will act as a spatial disturbance, triggering the instabilities in the D–L mode, and the thin thickness of the flames is responsible of the small size of the cells.

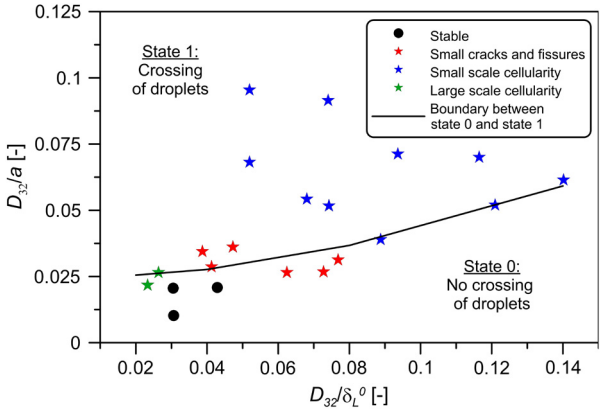

Fig. 16. Repartition of the different types of two-phase flame morphologies shown in Fig. 15 with the boundary of crossing/no crossing of the fuel droplets in the flame front.

Stable two-phase flames are located in the zone for which all fuel droplets are vaporized during flame propagation. Diluted sprays with very low droplet diameters, owing to their low values of D_{32}/a and D_{32}/δ_L^0, are reached for these cases, which explains that the fuel droplets are easily vaporized. However, some cases of unstable flames are found in the zone of no crossing of droplets. The large scale cellularities (green stars) and some instabilities with small cracks (red stars) are found for the no-crossing-droplet zone, which somewhat question the D–L mode to explain these cellularities. Moreover, the large scale cellularities are obtained with conditions very near to those found for the stable cases (green stars and black points), more specifically, with very small droplets size.

6.2. Interpretation of front patterns in terms of Darrieus–Landau instability

As recalled above, it is known that the patterns adopted by the D–L instability depend on the lateral extent of the flame and on the strength of the perturbations. We have hence to underline that the present experiments correspond to a domain much larger than the one involved in the numerical simulations reported above. Another difference is the geometry (expanding spherical flames), which is known to maximize the role of the hydrodynamic instabilities. To cope with such difficulties, several model equations have been proposed by Sivashinsky for studying further the Darrieus–Landau instability (see, for instance, [39]). Even though these models appear oversimplified in comparison with the conservation laws for a reactive systems, they allow one to simulate flame extents of more realistic size. Both approaches play a complementary role with results in agreement with each other, as performed in [35] where the DNS approach and the Sivashinsky non-linear model equation have been used to study the Darrieus–Landau instability with droplets.

For the single-phase flame in spherical expansion, the issue of the various front patterns has consequently been addressed with the use of model equations. Particularly interesting results have been obtained in [40], where the numerical simulation exhibits patterns of cells similar to those in the present experiments. Furthermore, the authors verified that the critical radius for the appearance of cells depends in a very important way on the noise amplitude. Actually, in the expanding spherical geometry, any source of noise (presence of droplets, turbulence) is able to trigger the Darrieus–Landau instability, its critical radius for the appearance depending on the amplitude and the type of noise.

The experimental results demonstrate that the presence of droplets is a very efficient mechanism (probably more efficient than turbulence in a number of cases) for triggering the D–L instability. When the droplets evaporate inside the flame thickness, the disturbance is of course a much less efficient forcing mechanism than when droplets cross the flame front, since they are of larger size. Moreover, disturbances of weak intensity require a large lateral domain to trigger the D–L instability, leading to large-scale cells. Consequently, the crossing/non-crossing line of Fig. 16 represents a limit where the forcing of instabilities by droplets becomes ineffective, leading in some cases to the appearance of large cell pattern, or to non-visible cells at a radius limited in our experiments at about 20 mm.

7. Conclusion

The ethanol/air spray system has been studied by both experimental and numerical means. The experiment is based on a spherical combustion chamber that uses the principle of the Wilson cloud chamber to create and control the spray. On the numerical side, the spray is schematized by a 2-D face-centred lattice of fuel droplets, located at the nodes and surrounded by an initial gaseous mixture of ethanol vapour and air.

A large part of the paper is devoted to characterize and analyse the most striking effect presently related to spray flames: the spray flames exhibit a strongly corrugated front pattern, while the equivalent single-phase flame does not in the same conditions. The same phenomenon of flame wrinkles and foldings is also observed in the numerical simulations, that permit to identify the front pattern exhibited numerically as of Darrieus–Landau (DL) type. It is furthermore shown

that the perturbations induced by the droplets trigger the DL-instability. This set of features allows us to explain why the DL-instability affect spray flames and not the equivalent single-phase spray flame.

A quantitative comparison between both experimental and numerical spray-flame speed is then conducted. The experimental results shows that the spray-flame speed is of the same order than the single-phase premixed flame. The numerical simulation of the flat spray flames indicates that the vaporization time plays a role in propagation and that the numerical spray-flame speed is smaller than in the reality. To explain this discrepancy, we invoke the speed-up produced by the Darrieus–Landau instability, which can increase the flat spray-flame speed by up to 50%.

Finally, we have presented the various front patterns created by the instability. The experiment indicates that large-scale front patterns are mostly related to droplets of moderate size, while spray flame fronts with small cells correspond to droplets of larger size. Theses features are interpreted in the light of what is already known about the role of the disturbances on the D–L instability affecting the premixed flames.

Acknowledgements

The present work has received the support of the Research Program “Micropesanteur fondamentale et appliquée”, GDR CNRS No. 2799, under contract CNES/150515.

References

[1] D. Ballal, A. Lefebvre, Flame propagation in heterogeneous mixtures of fuel droplets, fuel vapor and air, Proc. Combust. Inst. 18 (1981) 321–328.
[2] G. Myers, A. Lefebvre, Flame propagation in heterogeneous mixtures of fuel drops and air, Combust. Flame 66 (1986) 193–210.
[3] E. Cekalin, Propagation of flame in turbulent flow of two-phase fuel–air mixture, Proc. Combust. Inst. 8 (1961) 1125–1129.
[4] Y. Mizutani, A. Nakajima, Combustion of fuel vapor-drop-air systems part I: open burner flames, Combust. Flame 20 (1973) 343–350.
[5] Y. Mizutani, A. Nakajima, Combustion of fuel vapor-drop-air systems part II: spherical flames in a vessel, Combust. Flame 20 (1973) 351–357.
[6] S. Hayashi, S. Kumagai, Flame propagation in fuel droplet-vapor-air mixtures, Proc. Combust. Inst. 15 (1975) 445–451.
[7] S. Hayashi, S. Kumagai, T. Sakai, Propagation velocity and structure of flames in droplet vapor air mixtures, Combust. Sci. Technol. 15 (1976) 169–177.
[8] C. Polymeropoulos, S. Das, The effect of droplet size on the burning velocity of kerosene-air sprays, Combust. Flame 25 (1975) 247–257.
[9] F. Atzler, F.X. Demoulin, M. Lawes, Y. Lee, N. Marquez, Burning rates and flame oscillations in globally homogeneous two-phase mixtures (flame speed oscillations in droplet cloud flames), Combust. Sci. Technol. 178 (12) (2006) 2177–2198.
[10] H. Hanai, K. Maruta, H. Kobayashi, T. Niioka, Pulsating flame propagation of PMMA particle cloud in microgravity, Proc. Combust. Inst. 27 (1998) 2675–2681.
[11] S. Suard, P. Haldenwang, C. Nicoli, Different spreading regimes of spray flames, C. R. Mecanique 332 (5–6) (2004) 387–396.
[12] C. Nicoli, P. Haldenwang, S. Suard, Analysis of pulsating spray-flames propagating in lean two-phase mixtures with unity Lewis number, Combust. Flame 143 (2005) 299–312.
[13] D. Bradley, M. Lawes, S. Liao, A. Saat, Laminar mass burning and entrainment velocities and flame instabilities of isooctane, ethanol and hydrous ethanol/air aerosols, Combust. Flame 161 (6) (2014) 1620–1632.
[14] R. Thimothée, C. Chauveau, F. Halter, I. Gokalp, Characterization of cellular instabilities of a flame propagating in an aerosol, in: ASME Turbo Expo 2015: Turbine Technical Conference and Exposition, American Society of Mechanical Engineers, Montreal, Quebec, Canada, June 15–19, 2015, http://dx.doi.org/10.1115/GT2015-44022.
[15] H. Nomura, I. Kawasumi, Y. Ujiie, J. Sato, Effects of pressure on flame propagation in a premixture containing fine fuel droplets, Proc. Combust. Inst. 31 (2007) 2133–2140.
[16] H. Nomura, M. Koyama, H. Miyamoto, Y. Ujiie, J. Sato, M. Kono, S. Yoda, Microgravity experiments of flame propagation in ethanol droplet vapor air mixture, Proc. Combust. Inst. 28 (2000) 999–1005.
[17] C. Nicoli, B. Denet, P. Haldenwang, Rich spray-flame propagating through a 2-d lattice of alkane droplets in air, Combust. Flame 162 (2015) 4598–4611.
[18] C. Nicoli, B. Denet, P. Haldenwang, Spray-flame dynamics in a rich droplet array, Flow Turbul. Combust. 96 (2016) 377–389.
[19] F. Atzler, Fundamental Studies of Aerosol Combustion, Ph.D. thesis, School of Mechanical Engineering, University of Leeds, UK, 1999.
[20] M. Nassouri, C. Chauveau, F. Halter, I. Gökalp, Flame structure of ethanol-air premixed mixtures at high pressures in microgravity, in: Proceedings of ECM2013, Lund, Sweden, 2013.
[21] C.T.R. Wilson, On a method of making visible the paths of ionising particles through a gas, Proc. R. Soc. Lond. A 85 (578) (1911) 285–288.
[22] T. Tahtouh, F. Halter, C. Mounaïm-Rousselle, Measurement of laminar burning speeds and Markstein lengths using a novel methodology, Combust. Flame 156 (9) (2009) 1735–1743.
[23] A. Kelley, C. Law, Nonlinear effects in the extraction of laminar flame speeds from expanding spherical flames, Combust. Flame 156 (9) (2009) 1844–1851.
[24] R. Thimothée, C. Chauveau, F. Halter, I. Gökalp, Experimental investigation of the mechanisms of cellular instabilities developing on spherical two-phase flames, in: 13th International Conference on Liquid Atomization and Spray Systems, 2015.
[25] W. Brevis, Y. Niño, G. Jirka, Integrating cross-correlation and relaxation algorithms for particle tracking velocimetry, Exp. Fluids 50 (1) (2011) 135–147.
[26] H. Yu, W. Han, J. Santner, X. Gou, C.H. Sohn, Y. Ju, Z. Chen, Radiation-induced uncertainty in laminar flame speed measured from propagating spherical flames, Combust. Flame 161 (11) (2014) 2815–2824.
[27] M. Mikami, H. Oyagi, N. Kojima, Y. Wakashima, M. Kikuchi, S. Yoda, Microgravity experiments on flame spread along fuel-droplet arrays at high temperatures, Combust. Flame 146 (2006) 391–406.
[28] S. Aggarwal, W. Sirignano, Unsteady spray flame propagation in a closed volume, Combust. Flame 62 (1985) 69–84.
[29] I. Silverman, J. Greenberg, Y. Tambour, Stoichiometry and polydisperse effects in premixed spray flames, Combust. Flame 93 (1993) 97–118.
[30] A. Neophytou, E. Mastorakos, Simulations of laminar flame propagation in droplet mists, Combust. Flame 156 (2009) 1627–1640.
[31] J. Reveillon, L. Vervisch, Analysis of weakly turbulent dilute-spray flames and spray combustion regime, J. Fluid Mech. 537 (2005) 317–347.
[32] M. Kikuchi, Y. Wakashima, S. Yoda, M. Mikami, Numerical study on flame spread of an n-decane droplet array in different temperature environment under microgravity, Proc. Combust. Inst. 30 (2) (2005) 2001–2009.
[33] C. Nicoli, P. Haldenwang, Analysis of one-step chemistry models for flame propagation in various equivalence ratio premixtures of high alkane-air, in: SPEIC10: Towards Sustainable Combustion, Tenerife, Spain, 2010.
[34] C. Nicoli, B. Denet, P. Haldenwang, Lean flame dynamics through a 2d lattice of alkane droplets in air, Combust. Sci. Technol. 186 (2) (2014) 103–119.
[35] C. Nicoli, P. Haldenwang, B. Denet, Darrieus–Landau instability of premixed flames enhanced by fuel droplets, submitted for publication.

[36] B. Denet, P. Haldenwang, A numerical study of premixed flames Darrieus–Landau instability, Combust. Sci. Technol. 104 (1995) 143–167.
[37] A.R. Kerstein, C.K. Law, Percolation in combusting sprays I: transition from cluster combustion to percolate combustion in non-premixed sprays, Symp. (Int.) Combust. 19 (1) (1982) 961–969.
[38] N. Leplat, P. Dagaut, C. Togbé, J. Vandooren, Numerical and experimental study of ethanol combustion and oxidation in laminar premixed flames and in jet-stirred reactor, Combust. Flame 158 (4) (2011) 705–725.
[39] V. Karlin, G. Sivashinsky, Asymptotic modelling of self-acceleration of spherical flames, Proc. Combust. Inst. 31 (2007) 1023–1030.
[40] Y. D'angelo, G. Joulin, G. Boury, On model evolution equations for the whole surface of three-dimensional expanding wrinkled premixed flames, Combust. Theory Model. 4 (3) (2000) 317–338.